



A parametric study on the hydrodynamics of tidal turbine blade deformation

Federico Zilic de Arcos^{*}, Christopher R. Vogel, Richard H.J. Willden

University of Oxford. Department of Engineering Science, Parks Rd., OX1 3PJ, Oxford, UK

ARTICLE INFO

Article history:

Received 20 July 2021

Received in revised form 16 May 2022

Accepted 27 May 2022

Available online xxxx

Keywords:

Hydrodynamics

Axial-flow turbine

Fluid–structure interaction

Blade deformations

Tidal energy

ABSTRACT

The blades of axial-flow rotors, which are typically made of flexible composite materials, can experience significant deformations through their operation. However, the impact of these deformations on rotor hydrodynamics is not well understood. Blade deformations can be separated into three main components: flapwise, a thrust-driven deformation in the direction of the flow; edgewise, relatively small deformations in the plane of rotor motion and driven by rotor torque; and twist deformations that affect each blade's angle of attack distribution and are generated by the torsional moment acting about the blade's spanwise axis as well as by structural interactions. This work evaluates the hydrodynamic effects of the decoupled flapwise and twist deformations on a tidal turbine blade, using blade-resolved Computational Fluid Dynamics (CFD) simulations with the objective of identifying and quantifying the associated flow phenomena. The deformation cases were generated by scaling the static deformation shapes from a structural model of the turbine blade. The dataset used in this work, part of a larger research project, consists of 48 blade-resolved Reynolds-Averaged Navier–Stokes CFD steady-state simulations. It was found that twist deformation effects are significant, and can be adequately described using blade element theory. Flapwise deformations, on the other hand, produce different phenomena affecting the rotor loading and performance in ways that cannot be explained on a blade sectional basis through blade element theory. It is found that the hydrodynamic impact of flapwise deformations can be explained through two different mechanisms: a pressure drop on the suction side of the blade that generates inboard load augmentation, and an increase in near-tip radial flow effects that moves the onset of tip-loss effects, and shedding of thrust and power, further inboard. The studied cases show a significant impact of flapwise deformation on integrated power (up to a 20% drop), while the impact on integrated thrust remains limited, with variations between −4% to +2% in thrust coefficient observed depending on blade bending.

© 2022 The Author(s). Published by Elsevier Ltd. This is an open access article under the CC BY license (<http://creativecommons.org/licenses/by/4.0/>).

1. Introduction

The design and optimisation of turbine blades is a well studied area for which some established methodologies allow the designer to obtain optimised aero- or hydrodynamic geometries. These methods are typically based on Blade-Element Momentum Theory (BEMT) in which the flow through the turbine is discretised using a set of concentric annuli, and the

^{*} Corresponding author.

E-mail address: federico.zilic@eng.ox.ac.uk (F. Zilic de Arcos).

URL: <https://eng.ox.ac.uk/efm/> (R.H.J. Willden).

forces on each blade section described as a result of the incident relative flow-velocity and the two-dimensional polar characteristics of the foil section (Glauert, 1947; Burton et al., 2011). However, during operation, the blade geometry can deform due to the forces acting on the blade. These deformations can change the aero- or hydrodynamics of the blade, further affecting the forces acting on it and thus its deformation, driving fluid–structure interaction (FSI) phenomena.

Blade fluid dynamics are optimised for a range of different objectives. These include for open-flow operation, in the case of wind turbines (e.g. Chehouri et al. (2015)), farm optimisation or even local optimisations based on blockage and array configurations (e.g. Schluntz and Willden (2015)). These analyses typically assume the blade structure to be rigid, thus neglecting potential FSI effects and blade deformations which can be of significant magnitude. For example, Nicholls-Lee (2011) predicted a maximum tip deflection of 1.48 m for a 10 m radius tidal rotor; Grogan et al. (2013) predicted a maximum deflection of 1.75 m for a 12 m length tidal turbine blade; and Rafiee et al. (2016) a maximum deflection of 1.46 m for a 23.50 m radius wind rotor.

Efforts have been made to model the FSI phenomena on axial-flow rotors by solving the structural and fluid mechanics problems in parallel with varying degrees of complexity and coupling. The simplest approach and common engineering practice is to use one-way coupling methods, applicable where the deformations are deemed small and the resultant change in hydrodynamic loads due to these deformations negligible. The loads from an aero-/hydrodynamic solver are applied directly to a structural model to determine deformations or structural stress distributions (e.g. Bir (2001) and Grogan et al. (2013)) without iteration of the fluid loading. However, when the deformations are significant, two-ways coupled methods are better suited. In these methods, the deformed blade data from the structural solution is used within the fluid-dynamics solver to generate new loads, iterating until convergence is achieved (e.g. Bazilevs et al. (2011), Nicholls-Lee et al. (2013) and Rafiee et al. (2016)).

Amongst the different methods proposed to analyse the FSI phenomena on axial-flow rotors (Wang et al., 2016), lower-order models (e.g. models based on BEMT coupled with 1D structural beam elements) are generally desirable for practical applications. Such models typically have a sufficiently low computational cost that enables a large number of cases to be simulated, as required for the design and optimisation of commercial rotors. Engineering models for axial-flow turbine FSI have been developed and used in both academic and commercial environments (see e.g. Vorpahl et al. (2014), Guntur et al. (2016) and Larsen and Hansen (2007)).

Previous research by the authors has highlighted some limitations of the assumptions of blade-element theory that are fundamental for the aforementioned engineering models (Zilic de Arcos et al., 2019). Literature also suggests that a consensus regarding the fluid dynamics of rotor blade deformations has not yet been achieved. In the related area of wind energy, for example, investigations have been conducted for the similar fluid mechanics problem of coned rotors. Madsen and Rasmussen (1999) studied the hydrodynamic effects of out-of-plane coning and bending using an axisymmetric actuator-disc CFD approach, and showed how blade bending alters the axial and radial flow velocities through the disc. They demonstrated that the integrated power coefficient for the rotor is independent of the out-of-plane deflection for uniform rotor thrust loading. Mikkelsen et al. (2001), also using actuator-disc CFD simulations, observed that the power was reduced, but that the non-dimensional power coefficient based on the projected rotor area is largely unaffected by coning of the rotor. Mikkelsen et al. (2001) argue that the changes in radial flow cannot be captured by BEMT without violating the annular independence assumption of the theory. However, Crawford (2006) maintained the streamtube independence requirement to formulate a modified BEMT model for coned rotors, reporting power and thrust reductions across most of the span of a wind rotor. In contrast, the results presented by Zilic de Arcos et al. (2019), obtained through blade-resolved CFD simulations, showed increased loading around the inboard of a rotor blade bent in the flapwise direction. Ultimately, this lack of consensus presents difficulties for assessing the accuracy and scope of application of the available FSI engineering models for axial-flow rotors.

Passive rotor control through blade deformations seeks to exploit the FSI phenomena on axial rotors to achieve control objectives such as load and power shedding above rated flow speed (e.g. Wada et al. (2011), Murray et al. (2018) and Kaufmann et al. (2019)). These strategies often rely on large deformations that are expected to occur in a controlled manner, and their design and optimisation is likely to rely on engineering models. This area, however, is particularly affected by the aforementioned limitations on the understanding of deformed blade hydrodynamics. Such an understanding is not only a prerequisite for the accurate modelling of deformed rotor blades, but also for determining the feasible limits of passive control technologies.

This study seeks to identify and quantify the significance of the hydrodynamic effects of tidal rotor blade deformations, presenting the findings in terms that are relevant for the development and improvement of engineering models. The approach is to utilise a framework in which we decouple the deformations into three main components: flapwise deformation, driven by thrust forces and typically the largest deformation component in magnitude; edgewise deformation, driven by blade torque and typically small in comparison; and twist deformations that modify the spanwise twist angle distribution along the blade and are driven by the moment caused by structural coupling effects and the misalignment of the structural centre and the centre of pressure. These principal deformation components are depicted for a turbine blade in Fig. 1.

An extensive suite of blade-resolved Computational Fluid Dynamics (CFD) simulations are performed to investigate the impact of twist and flapwise deflections. The effect of deflection magnitude has been assessed parametrically based on the scaled static response from structural analysis of a composite tidal turbine blade (Zilic de Arcos et al., 2019). The blade geometry, designed by Schluntz and Willden (2015), modified by Wimshurst and Willden (2016) and Zilic de Arcos

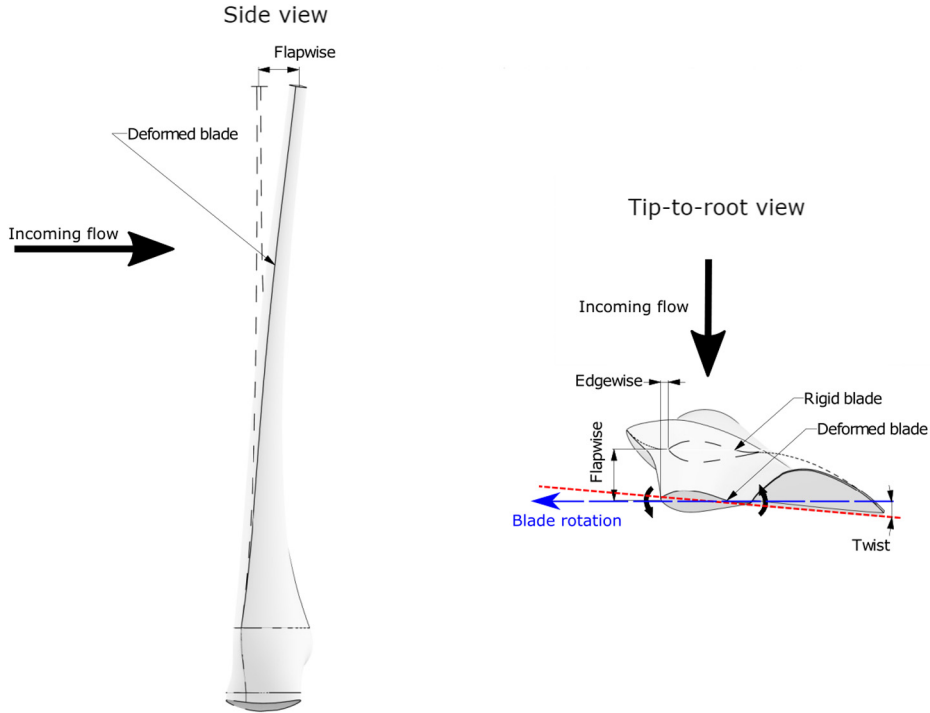


Fig. 1. Deformation degrees of freedom for a turbine blade as seen from side and blade tip-to-root views. The two views show a three-dimensional render of the deformed blade alongside an outline of the undeformed blade. The nacelle and the remaining blades have been omitted for clarity.

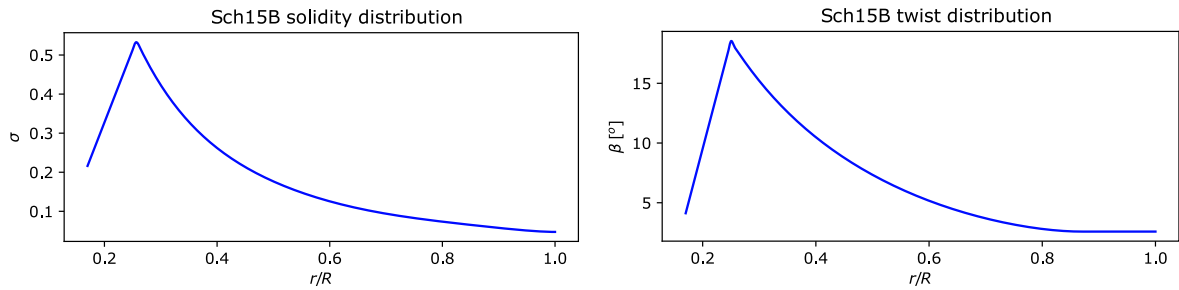


Fig. 2. Characteristics of the Sch15B rotor: Spanwise distributions of the blade solidity σ , and twist angle β .

et al. (2019), was simulated for 6 cases of twist-only deformation, and 5 cases of flapwise-only deformation. Each of these cases, in addition to a case with no deformation, were meshed and simulated at four different tip-speed-ratios λ each.

The resulting dataset was used in this work to identify the hydrodynamic effects associated with the decoupled deformations twist-only and flapwise-only, providing insights into the phenomena affecting forces and flow development, alongside with an understanding that can be later used to improve the accuracy and predictive capabilities of engineering models. This paper is focused only on the hydrodynamics of the individual flapwise and twist deformation cases. The analysis of coupled flapwise and twist deformations is to be presented in a subsequent publication.

2. Rotor characteristics

The rotor used in this study is a tidal turbine design developed by Schluntz and Willden (2015) for a blockage ratio (ratio of turbine swept area to surrounding flow passage cross-sectional area) of 0.197, and modified by Wimshurst and Willden (2016) and by Zilic de Arcos et al. (2019) in the root region. It is a three-bladed 20 m diameter rotor based on a single RISØ A1-24 aerofoil from 25% of the rotor radius to the blade tip and a transition surface from the aerofoil cross-section to a cylindrical root between 25% and 15% of the rotor radius, where the blade is attached to the nacelle. The aerofoil's quarter-chord is aligned with the blade's pitch axis. The distribution of twist angle β and solidity $\sigma = cN/(2\pi r)$ where c is the local chord, N the number of blades, and r the local radius, are shown in Fig. 2.

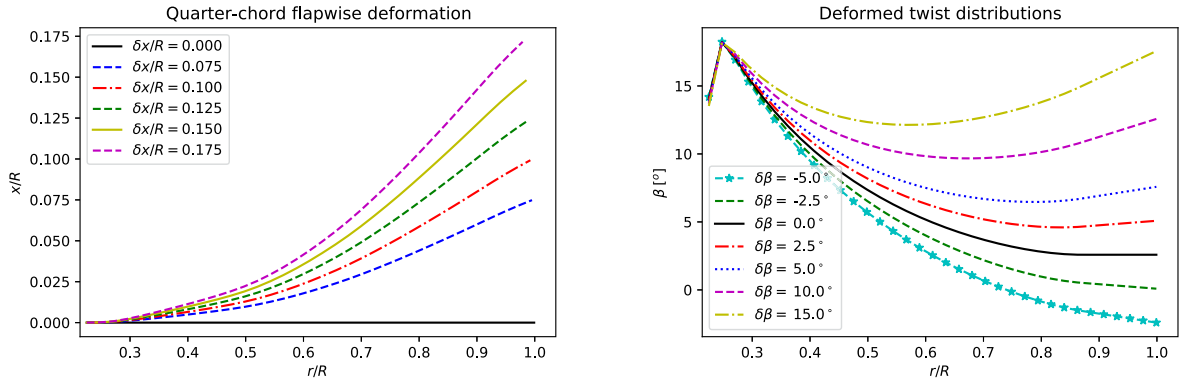


Fig. 3. Axial-position of the quarter-chord line for the different flapwise deformation cases $\delta x/R$ (left), and twist distributions for the twist deformation cases $\delta\beta$ (right).

Table 1

Testing matrix of simulated cases for $\delta\beta$ and $\delta x/R$. Each point in the matrix was simulated at tip-speed-ratios $\lambda \in [4.0, 5.0, 6.0, 7.0]$.

$\delta x/R$	$\delta\beta [^\circ]$						
	−5.0	−2.5	0.0	2.5	5.0	10.0	15.0
0.000	✓	✓	✓	✓	✓	✓	✓
0.075			✓				
0.100			✓				
0.125			✓				
0.150			✓				
0.175			✓				

The root region was modified from the original design as described in [Zilic de Arcos et al. \(2019\)](#) to provide a smoother geometrical transition from the aerofoil section to the circular coupling point at the nacelle, avoiding stress concentrations due to the abrupt cross-section change seen in earlier geometries.

3. Parametric space

The parameter space developed includes, in addition to the undeformed blade geometry, five flapwise-only deformation cases, and six twist-only deformation cases.

The twist deformation was applied as a linear function over the span of the blade, starting from no deformation at $0.25R$, with R the blade radius, to a value $\delta\beta$ at the tip, with the tip twist being used to label and identify the different cases. The use of a linear twist deformation distribution is a simplification of a complex fluid–structural phenomenon that involves the moment distribution over the blade, the position of the structural centre and the bending–twist coupling mechanisms ([Lobitz and Veers, 2003](#)). This simplification is supported as an approximation to the solution extracted from an engineering FSI model ([Zilic de Arcos et al., 2018](#)). The analysed cases are $\delta\beta \in [-5.0, -2.5, 0.0, 2.5, 5.0, 10.0, 15.0][^\circ]$.

The flapwise deformation was generated by scaling the flapwise component of the static deflection of the quarter-chord line as extracted from the shell-element structural model in [Zilic de Arcos et al. \(2018\)](#) at a tip-speed-ratio of $\lambda = 5.5$ and a flow speed of $V_\infty = 4.5$ [m/s]. This specific case was chosen to form the flapwise deformation mode, as it exhibited negligible twist deformations. The flapwise deformation cases are labelled and identified by the flapwise deformation value at the tip, $\delta x/R$, with the cases analysed being $\delta x/R \in [0.000, 0.075, 0.100, 0.125, 0.150, 0.175]$. The flapwise deformations resulted in a small reduction in the rotor radius projected onto the streamwise plane that corresponds to 0.00%, 0.27%, 0.52%, 0.83%, 1.13%, and 1.22% of the undeformed rotor radius, respectively. These reductions correspond to a reduction of 0.53% for the projected swept area for the $\delta x/R = 0.075$ case, up to 3.30% for $\delta x/R = 0.175$.

The blade surfaces were constructed using the Algorithmic-Aided Design package Rhinoceros 6.0 with Grasshopper 1.0. The different blade geometries were built by interpolating NURBS surfaces over 100 transverse sections, controlling the individual twist angle of each section, and specifying the required deformation values.

Each of the aforementioned cases were simulated at four tip-speed-ratios $\lambda = \omega R/V_\infty$, with ω the rotational speed and V_∞ the undisturbed flow velocity. The simulated tip-speed-ratios were $\lambda \in [4.0, 5.0, 6.0, 7.0]$, simulated by varying the rotational speed, and completing a stencil of 48 blade-resolved CFD simulations used to build the dataset. The spanwise twist distribution of the twist-deformation cases, as well as the deformed quarter-chord line for the flapwise deformation cases described above can be seen in [Fig. 3](#). A summary of the simulation case matrix is provided in [Table 1](#).

4. CFD model

4.1. Model details

The cases were modelled with a Reynolds-Averaged Navier Stokes (RANS) CFD approach under incompressible steady-state assumptions using the commercial solver Fluent 19.0. The closure of the RANS equations was made through the $k - \omega$ SST turbulence model (Menter, 1994) with the updated constants of Menter et al. (2003) and a blending-function wall-modelling approach (Fluent, ANSYS, 2018). This model selection is supported by the work of McNaughton et al. (2012) and Afgan et al. (2013) where they show this turbulence closure model to agree well with experiments and higher-order turbulence closure models. A cell-centred finite volume discretisation scheme was used with a second-order upwind spatial discretisation and a coupled-pressure algorithm, which provides robustness and efficiency in single phase flows under steady-state conditions (Fluent, ANSYS, 2018).

To model the turbine rotation under steady-state conditions we used the Multiple Reference Frame model described by Luo and Gosman (1994) with a rotatory region for the turbine and stationary region for the remainder of the control volume, each region having a different rotational speed ω defined by its local frame of reference. Across the interface, reference frame transformations are performed to enable the transport of fluxes from one sub-domain to another, as described in the original reference.

The entire domain was modelled using a cylindrical control volume, exploiting the rotational symmetry of the problem and modelling only one blade in a 120° wedge with periodic boundary conditions along the azimuthal boundaries ($x - r$ planes). The remaining boundary conditions were defined as: velocity inlet with a uniform speed of 4.5 m/s with a turbulence intensity of 10% and a length scale of 0.7 times the rotor diameter, following Wimshurst and Willden (2016) and based on data presented by Gant and Stallard (2008); the rotor blade surfaces as non-slip smooth walls; the outlet by a constant-pressure equal to that of the undisturbed flow, and the outer-cylindrical domain surface defined with a symmetry condition. Finally, the internal sub-domain interfaces are non-conformal.

The outer domain was modelled with a radius of 10 times the rotor radius to minimise blockage effects (blockage ratio 1%), with a length upstream equal to 5 times the rotor radius and 14 radii downstream. These dimensions provide sufficient space for flow development without undue influence of the boundaries on rotor performance or flow behaviour, as described by Wimshurst and Willden (2016).

This modelling approach was selected as it provides accurate blade-resolved results and reduces the computational time by exploiting symmetry and steady-state conditions. A full validation of the methodology is presented in Wimshurst and Willden (2017b), where comparisons of blade resolved wind turbine CFD results and the MEXICO experiments (Schepers et al., 2012; Boorsma and Schepers, 2014) are provided in terms of spanwise force distributions and sectional pressure coefficients.

The simulations were performed on the ARCUS HPC facilities at the University of Oxford. For each simulation the solver iterated 20,000 times running on 96 cores and reducing the scaled residuals by at least 6 orders of magnitude for the continuity and velocity components, and at least 5 orders for the turbulence scalars.

4.2. Mesh study

Structured meshes were prepared for this study based on previous numerical studies, building a different mesh for each of the deformation cases described in Section 3. The general mesh topology, presented by Zilic de Arcos et al. (2019), consists of a Y-grid general layout and an O-grid mesh around the blade surfaces, following the geometries defined by the parametrically-generated NURBS surfaces.

The meshes of the different cases maintained a very similar near-blade region, providing good resolution of the near-wall flow features, and adapting buffer regions upstream and downstream of the rotor plane to absorb the deformations, with the number of elements n_c remaining constant. The non-dimensional wall distance y^+ was kept within the wall-modelling region (i.e., $30 \leq y^+ \leq 300$). The near-wall O-grid region has a first-layer thickness close to the blade surfaces of $\Delta y = 2.5 \times 10^{-4}$ m (giving $8.5 \times 10^{-5} \leq \Delta y/c \leq 2.5 \times 10^{-4}$ along the blade), a wall normal growth-rate of 1.05 over 25 layers that smoothly transitions to the rest of the domain.

The original rotor subdomain (Zilic de Arcos et al., 2019) was modified to accommodate the blade deformations, and so a new mesh convergence study was performed. Three different turbine meshes were simulated at the highest thrust condition, $\lambda = 7.0$, as this presents the most sheared, and therefore most numerically demanding, flow condition. A subsequent refinement factor k_i of 2.0 was applied in each linear element dimension.

To assess the numerical uncertainty of the simulations, the grid-convergence index (GCI) described by Roache (1994) and a relative error measure between meshes were used. The relative error E_R is defined as:

$$E_{R,i} = (\xi_i - \xi_{i-1})/\xi_i \quad (1)$$

with ξ is the analysed variable and the subscripts i and $i - 1$ correspond to the current and coarser meshes, respectively. The analysed variables for this mesh study are the integrated power and thrust coefficients:

$$C_p = \frac{\omega \tau}{1/2 \rho A V_\infty^3} \quad (2)$$

Table 2

Mesh sensitivity analysis for the turbine domain, where n_c is the number of elements, k_i the refinement factor, E_R the relative error between two meshes, and GCI the grid convergence index.

# of elements	Refinement factor	Thrust			Power		
		C_T [-]	E_R [%]	GCI [%]	C_P [-]	E_R [%]	GCI_i [%]
n_c	k_i						
0.70M	1.00	1.024	–	–	0.297	–	–
5.41M	2.00	1.064	3.72	1.54	0.345	13.95	0.99
43.28M	4.00	1.059	–0.50	0.54	0.344	–0.32	0.35
∞	∞	1.062	0.00	0.00	0.344	0.00	0.00

$$C_T = \frac{T}{1/2\rho AV_\infty^2} \quad (3)$$

with τ the integrated rotor torque, T the integrated rotor thrust and A the undeformed turbine's cross-sectional frontal area.

The coarse mesh was found to be outside the asymptotic convergence range, and so the GCI was only calculated for the medium and fine meshes, using an estimated effective order for the numerical method of $\mathcal{O} = 1.50$ based on previous observations (Zilic de Arcos et al., 2020a) and a safety factor of 2 (Roache, 1994) (see Table 2). Using GCI , the numerical uncertainty of the medium mesh shows a maximum relative error of 0.5% with respect to the fine mesh, and its uncertainty is estimated to be a conservative 1.54%. Thus, we consider the medium mesh appropriate to conduct the parametric study.

4.3. Flow field post-processing

The results of the CFD simulations are presented in terms of the spanwise distributions of forces in the axial, tangential and radial directions, F_x , F_θ and F_r , respectively, and with the flow-field analysis performed using the Streamtube Analysis Method (SAM) developed by Hunter (2015) and reviewed by Zilic de Arcos et al. (2020b). SAM works by sampling the flow-field over a series of concentric streamtubes centred around the rotor axis, with each crossing the rotor at a different radial location, to develop the spanwise variation in flow-field parameters, such as axial or tangential flow speed at the rotor. Each streamtube may expand or contract in the stream direction, as required by mass conservation, and the flow at each streamwise position is azimuthally averaged for analysis.

The spanwise force distributions $\vec{F} = [F_x, F_\theta, F_r]$ are obtained by integrating the pressures and shear forces over C , the blade cross-section at radius r , according to the following equation, in which p is the pressure, \vec{n} is the unitary surface-normal vector, and \vec{S} the wall shear stress vector.

$$\vec{F}(r) = \oint (p\vec{n} + \vec{S})dC \quad (4)$$

The SAM method is used to extract the angles of attack $\alpha(r)$ from the simulations through reconstructed azimuthally-averaged streamtubes where:

$$\alpha = \phi - \beta \quad (5)$$

and $\phi(r)$ is the angle of the local flow relative to the rotor plane, and $\beta(r)$ is the blade's geometric twist at radius r , as shown in Fig. 4. Here, $\phi(r)$ is calculated including the influence of the blade on the flow, and sampled directly from the CFD results:

$$\phi = \tan^{-1} \left(\frac{V_x}{V_\theta} \right) \quad (6)$$

with V_x and V_θ the axial and tangential velocities, respectively.

The flow velocities are extracted from the azimuthally-averaged streamtubes at a non-dimensional distance upstream and downstream of the rotor plane, $\Delta x/c$, from where Δx is measured in the local axial coordinate direction and c is the local chord. Unless otherwise stated in the corresponding results, a value of $\Delta x/c = 1.0$ was used, as this has previously been found to achieve parameter-independent results, as reported in Zilic de Arcos et al. (2020b).

The blade's local lift and drag coefficients, C_L and C_D , are calculated by projecting the axial and tangential forces F_x and F_θ in a frame of reference aligned with the flow incident on the blade W . The incident flow speed is itself determined through:

$$W(r) = \sqrt{V_x^2 + V_\theta^2} \quad (7)$$

Note that quantities normalised by area or blade radius (A and R) make use of the values that correspond to the undeformed rotor.

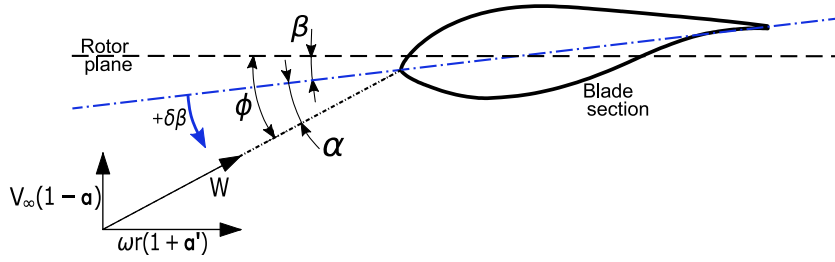


Fig. 4. Flow diagram over an arbitrary blade section, indicating the positive direction for twist deformations $\delta\beta$ (blue arrow). (For interpretation of the references to colour in this figure legend, the reader is referred to the web version of this article.)

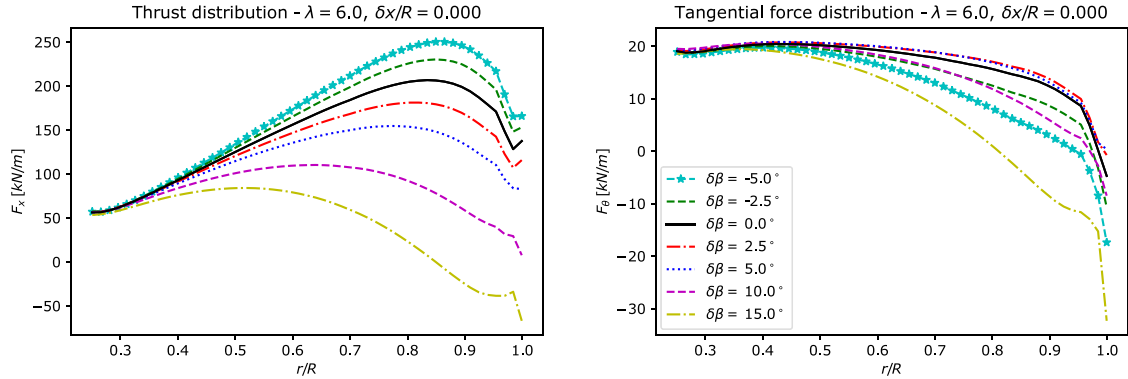


Fig. 5. Spanwise thrust (left) and tangential force (right) distributions for the rotor blade with twist only deformation at a tip-speed ratio $\lambda = 6.0$.

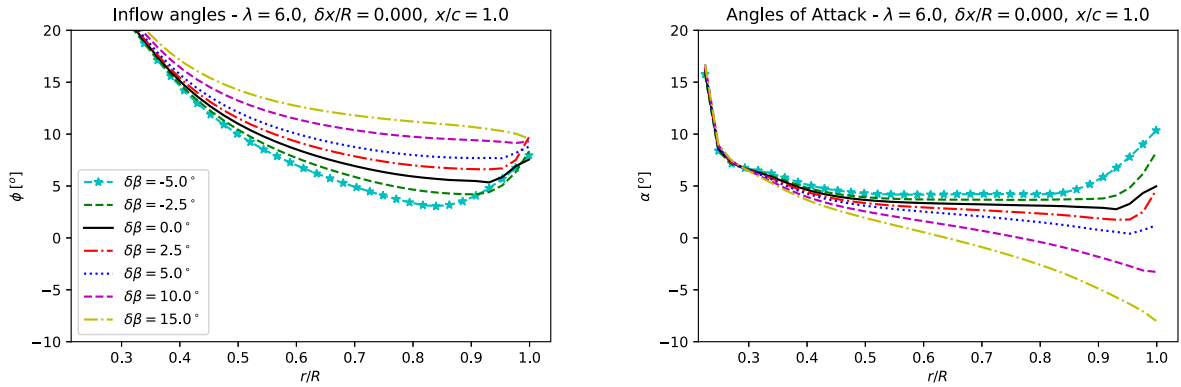


Fig. 6. Spanwise distributions of the flow angle ϕ (left) and angle of attack α (right) for the rotor blade with twist only deformation at a tip-speed ratio $\lambda = 6.0$.

5. Results and discussion

5.1. Twist deformation analysis

Fig. 5 shows the variations in thrust and tangential force caused by the twist deformation for the different $\delta\beta$ deformation cases, with the turbine operating at a tip-speed ratio $\lambda = 6.0$, while Fig. 6 shows the changes in the flow angles ϕ and angles of attack α for those same cases.

From the results, we observe that increases in $\delta\beta$, i.e., deformation towards feather, reduce the angle of attack, with an attendant reduction in thrust force, while a negative $\delta\beta$, i.e., deforming towards stall, produces the opposite effect. The thrust changes due to $\delta\beta$ can be explained following the projection of the local thrust and tangential force coefficients

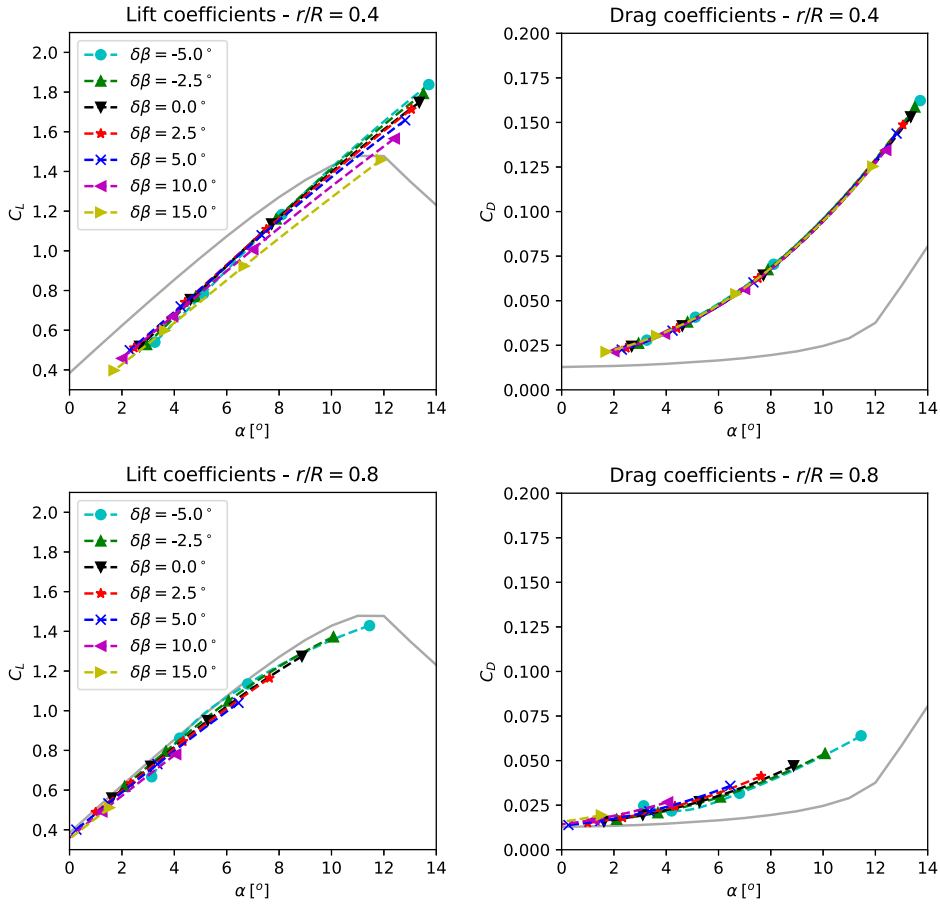


Fig. 7. Sectional lift and drag coefficients at two radial locations for different twist deformation cases. Sectional data are extracted from blade resolved simulations, in which each simulated tip-speed ratio λ provides data for a single angle of attack α at each spanwise location. The grey line corresponds to the two-dimensional lift and drag coefficients.

(C_X and C_θ respectively), in terms of the sectional lift and drag coefficients (C_L and C_D):

$$C_X = C_L(\alpha) \cos \phi + C_D(\alpha) \sin \phi \quad (8)$$

$$C_\theta = C_L(\alpha) \sin \phi - C_D(\alpha) \cos \phi \quad (9)$$

For small ϕ , as occurs across the mid and outboard sections of the blade, $\cos \phi \approx 1$ and $\sin \phi \approx \phi$. In addition, $C_L \gg C_D$ at small angles of attack for a typical aerofoil and Eq. (8) is thus dominated by the first term. It follows for the attached-flow regime that the thrust coefficient can be approximated as $C_X \approx C_L(\alpha)$ for the mid and outboard sections of the blade span, which accounts for the changes in thrust displayed in Fig. 5.

The changes in tangential force are more complex, since Eq. (9) is not necessarily dominated by either of the lift or drag terms. We observe in Fig. 5 that the tangential force drops in most cases, which is attributed to the local aerofoil operating away from its design conditions. However, a slight increase in the tangential force component is observed along the entire blade span for twist angle cases of 2.5° and 5.0° . This increase in tangential force is due to non-linearity and that the change in $\delta\beta$ does not manifest just as the change in angle of attack seen in Fig. 6, but also as an alteration to the inflow angle ϕ . Specifically for the $\delta\beta = 2.5^\circ$ and $\delta\beta = 5.0^\circ$ cases, a smaller angle of attack leads to a reduction in C_L and C_D , but also to an increase in ϕ . The consequence is that, for the $\delta\beta = 2.5^\circ$ and $\delta\beta = 5.0^\circ$ cases, the changes in the trigonometric functions in Eq. (9) offset the changes in the lift and drag coefficients, leading to higher torque but smaller thrust forces.

In Fig. 7 we analyse the changes in aerofoil characteristics extracted from the rotor simulations. Each simulated tip-speed ratio is analysed at a set of radial locations, and at each radial location the actual angle-of-attack, relative inflow speed, and resultant sectional lift and drag coefficients are determined. By looping over the tip-speed ratios simulated we are then able to reconstruct lift and drag coefficient curves as a functional of angle-of-attack for each radial location.

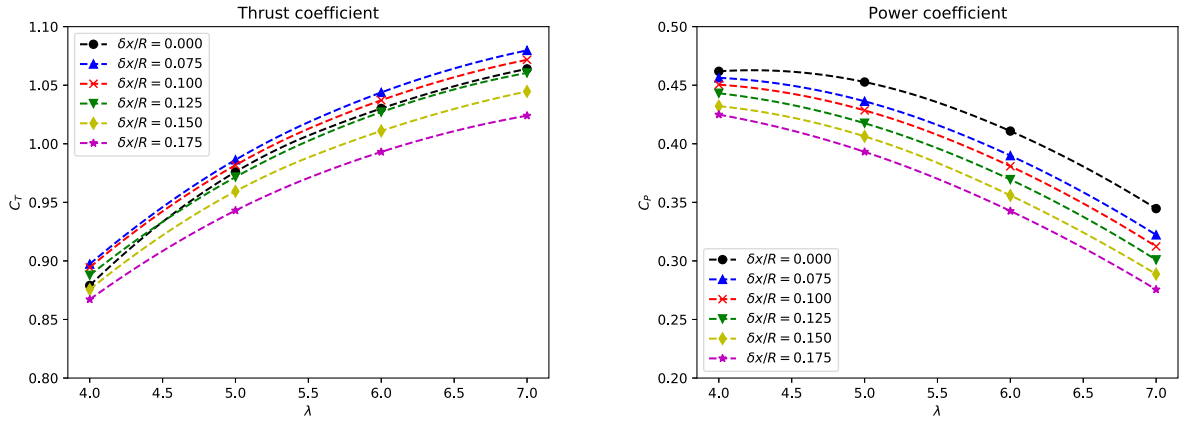


Fig. 8. Integrated thrust (left) and power (right) coefficients for different flapwise deformations. The coefficients are normalised by the undeformed rotor swept area.

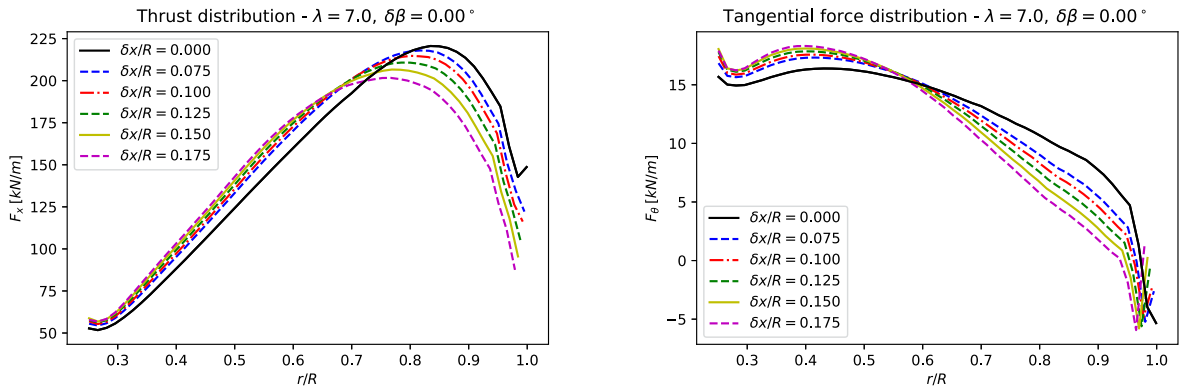


Fig. 9. Spanwise thrust (left) and tangential force (right) distributions for the rotor blade under flapwise deformation only at a tip-speed ratio $\lambda = 7.0$.

In contrast to the flapwise deformation cases to be discussed in the following section (Section 5.2), we observe relatively small changes in the aerofoil's lift and drag coefficients arising from blade twist deformations, especially in comparison to the larger differences observed at different radial positions, as shown in Fig. 7. We observe that most deformation cases converge with each other over a narrow spread for both lift and drag, although a maximum spread of approximately 9% in lift for the largest deformation cases ($\delta\beta = 10.0^\circ$ and $\delta\beta = 15.0^\circ$), highest angle of attack and closer to the root is observed. We attribute the larger spread to three-dimensional flow effects close to the transitional sections around the root ($0.15 \leq r/R \leq 0.25$), pre-stall effects, and to the analysis methodology itself, and not necessarily to strong variations caused by deformation.

Changing the radial coordinate affects the polar coefficients more significantly than twist deformation. For the cases analysed in Fig. 7, the drag coefficient shows relative differences up to approximately 100% at the highest angle of attack, although with a similar change in lift in absolute terms. On the lift coefficients, a stall delay is also observed closer to the root at the highest angles of attack. The changes in the two-dimensional polars over the blade span, while significant, are a phenomenon that has been widely discussed in literature (see e.g., [Wimshurst and Willden \(2017b\)](#)) and will not be further discussed as it falls outside the scope of this work.

Finally, we conclude from these observation that the changes in force distributions caused by twist deformations can be explained through variations in the local velocity triangle (i.e., mostly due to changes in the inflow angles and angles of attack) as well as angle of attack-related changes to the blade two-dimensional lift and drag coefficients, $C_L(\alpha)$ and $C_D(\alpha)$.

5.2. Flapwise deformation analysis

The flapwise deformation hydrodynamic effects are more complex to analyse than the effects of twist deformation as the annular independence assumed in blade-element momentum theory is violated by the development of spanwise flows along the blade, and hence the changes in forces cannot be simply explained by changes in angles of attack.

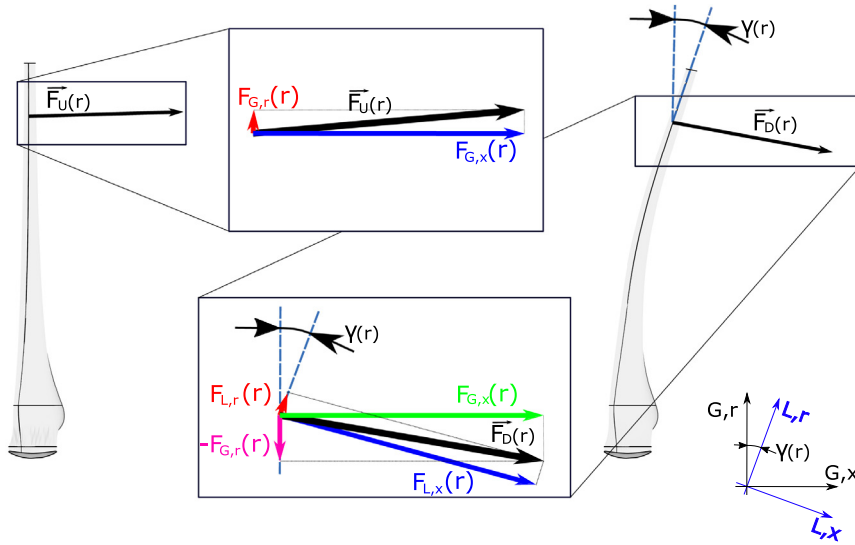


Fig. 10. Diagram comparing the axial and radial forces acting on undeformed (left) and deformed (right) blades. The forces on the undeformed case ($F_U = [F_{G,x}, F_{G,r}]$, where x and r stand for axial and radial components, respectively, and G for the global frame of reference) are equal in both the local and global frames of reference. On the deformed blade, the resulting force vector \vec{F}_D is decomposed in both the global and local (components with the L index) frame of reference, with γ the deflection angle. Diagram not to scale.

Fig. 8 shows the thrust and power coefficients for the whole rotor, normalised by the momentum and kinetic energy flux through the undeformed rotor swept area respectively. The coefficients show the impact of flapwise deformation on power and thrust. Increasing flapwise deformations produce an increasing reduction in C_p , with a maximum power loss of approximately 20% for the largest deformation case. On the contrary, flapwise deformations show a smaller impact on thrust coefficient, with an increase in C_T for modest flapwise deformations (ca. +2%), and a reduction in C_T for larger deformations (maximum of approximately -4% for the largest deformation). These effects, especially on power coefficient, are considerably larger than the modest modifications to rotor swept area that occur as a consequence of flapwise deformations. The variations in the frontal swept area are in the range of 0.53% to 3.3%, for $\delta x/R = 0.075$ to $\delta x/R = 0.175$ cases, as described in Section 3.

From the force distributions in Fig. 9, presented for the different flapwise-deformation cases, we observe how the deformed cases exhibit increased loading in the inboard region of the blade where the flapwise deformations are small, and increased load shedding near the tip, which resembles a tip-loss effect but with increased magnitude and radial variation. These changes in spanwise force distribution are associated with two different effects acting on the blade which are discussed in the following sections: a decrease in static pressure on the suction side of the blade that results from radial flow expansion (Section 5.2.1), and an increased radial loss that moves the onset of tip-loss effects inboard towards the blade root (Section 5.2.2). Although these changes result from three-dimensional flow effects, it is also instructive to interpret the flow-field changes in terms of changes to two-dimensional sectional blade characteristics which we present in Section 5.2.3.

5.2.1. Inboard load augmentation

An undeformed blade projects a very small radial-area as viewed along the radial axis from the blade tip. As the flapwise deformation increases so too does this radial-area projection, and due to the pressures acting on the blade surfaces, the blade starts to act as a significant source of radial momentum to the flow.

For the undeformed case, we observe a small radial fluid force that acts on the blade in the same (outwards) direction as the centrifugal forces, i.e., $F_{G,r} > 0$, see Fig. 10 for definitions. As the tip deformation δx increases the local radial force, $F_{L,r}$, as well as the local thrust force, $F_{L,x}$, are rotated by an angle, $\gamma(r)$, corresponding to the tangent of the deformed quarter-chord line, as shown in Fig. 10. This leads to a significant force component in the global radial direction, $F_{G,r}$, that acts on the blades towards the nacelle, as shown in Fig. 11.

If changes to the flow streamlines are negligible as the blade bends, the radial and thrust forces on the flapwise-deformation case can be estimated by projecting the undeformed case axial and radial forces onto the rotated quarter-chord line of the flapwise-deformed case, as described before:

$$F_{G,x} \approx F_{L,r} \cdot \sin \gamma + F_{L,x} \cdot \cos \gamma \quad (10)$$

$$F_{G,r} \approx F_{L,r} \cdot \cos \gamma - F_{L,x} \cdot \sin \gamma \quad (11)$$

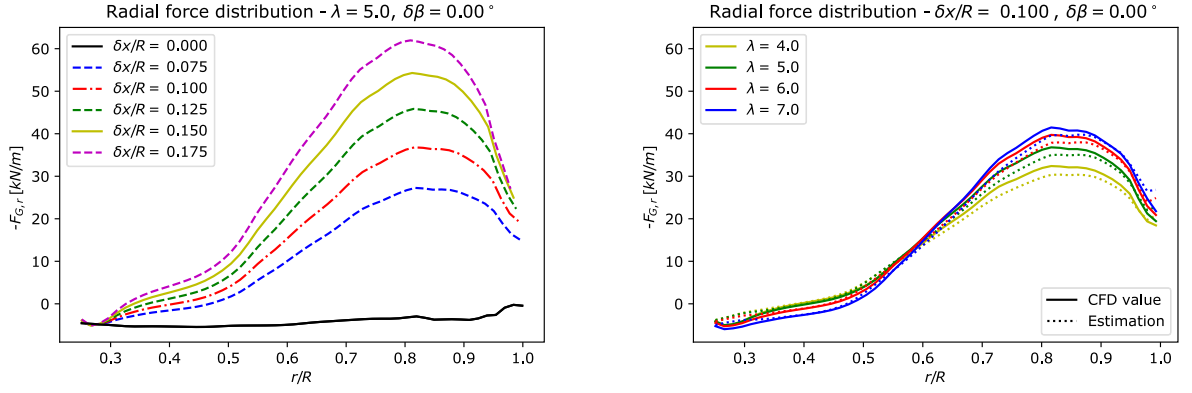


Fig. 11. Spanwise radial force distribution for various tip deflections $\delta x/R$ (left) and comparison between the spanwise force distribution extracted from the deformed blade CFD results and an approximation based on the vectorial projection of the undeformed force vector onto the local frame of reference of a deformed blade, for different tip-speed ratios (right). Both plots correspond to cases under flapwise deformation only.

with $F_{G,x}$ and $F_{G,r}$ the estimated thrust and radial forces referenced to the global frame of reference for a flapwise-deformed case, $F_{L,x}$ and $F_{L,r}$ the thrust and radial forces from the undeformed case projected onto the local frame of reference (note that the local and global frames of reference are the same for the undeformed blade).

The radial forces predicted for the flapwise deformed blade using Eq. (11), which re-orientates the forces of the undeformed blade according to its shape, are compared with the radial forces from the deformed blade CFD simulations in Fig. 11. These plots show good agreement across large parts of the blade between the approximation, which neglects any feedback effects on the flow, and the deformed blade CFD extracted results, reaching a maximum integrated-load error of approximately 3% primarily due to discrepancies observed between $r/R = 0.6$ and $r/R = 0.9$. This demonstrates that the primary mechanism for generation of the radial component of the force acting on the blade is due to the reorientation of the thrust loading acting on the blade rather than from any changed radial flow physics.

The radial force experienced by the blade impacts the flow as it passes through the rotor. As the radial force on the blade is generally inboard, $F_{G,r} < 0$, the reaction experienced by the flow is in the outboard direction and results in an increase in radial momentum flux. Thus the flow expands radially as it passes through the rotor and an increase in radial velocity is observed at the rotor plane as the blade deformation increases, as shown in Fig. 12. The increased radial momentum results in increased wake expansion which we visualise in Fig. 12 through the streamtube expansion past the rotor for two cases, with an expanded wake being observed for all λ considered.

The force changes observed in the axial and tangential directions, cannot however be fully explained by the vectorial reorientation and decomposition applied to estimate the radial force. Following Eq. (10), significant axial loading changes would not be expected in the inboard regions of the blade for small flapwise deformations.

The load augmentation in the inboard regions is a consequence of wake expansion. Observing Fig. 12, which shows streamtubes for the $\delta x/R = 0.075$ and undeformed cases, the close comparability of the streamtube widths in the inboard region of the undeformed and deformed blades, both upstream of and through the rotor, along with equivalent conditions upstream, imply a similar mass flux through the inboard streamtubes of both rotors. It follows that:

$$U_{1,U} \approx U_{1,D} \quad (12)$$

with U_1 the through-rotor (turbine plane) velocity and the subscripts U and D representing the undeformed and flapwise-deformation cases respectively.

Downstream of the rotor the inboard streamtubes expand at different rates, resulting in greater wake expansion and a smaller wake velocity, U_2 , for the deformed blade cases. As the static pressure must recover back to the same undisturbed pressure p_∞ far downstream in both cases, this implies that the downstream total pressure is reduced in the deformed blade case. Applying Bernoulli's equation along a streamline downstream of the rotor into the far wake, we deduce that the static pressure is reduced on the downstream side, or suction surface, of the deformed blade:

$$\frac{1}{2}\rho U_1^2 = p_\infty - p^- + \frac{1}{2}\rho U_2^2 \quad (13)$$

where p^- is the pressure on the downstream side of the rotor, as described in classic momentum theory (Glauert, 1947). As p_∞ and U_1 remain unchanged (across inboard sections) between the undeformed and deformed blades we may then write:

$$\Rightarrow \frac{1}{2}\rho U_{2,U}^2 - p_U^- = \frac{1}{2}\rho U_{2,D}^2 - p_D^- \quad \text{or} \quad p_U^- - p_D^- = \frac{1}{2}\rho (U_{2,U}^2 - U_{2,D}^2) \quad (14)$$

and as $U_{2,U} > U_{2,D}$ it follows that a reduced static pressure is required when the blade deforms for energy conservation in the downstream control volume (i.e., $p_U^- > p_D^-$).

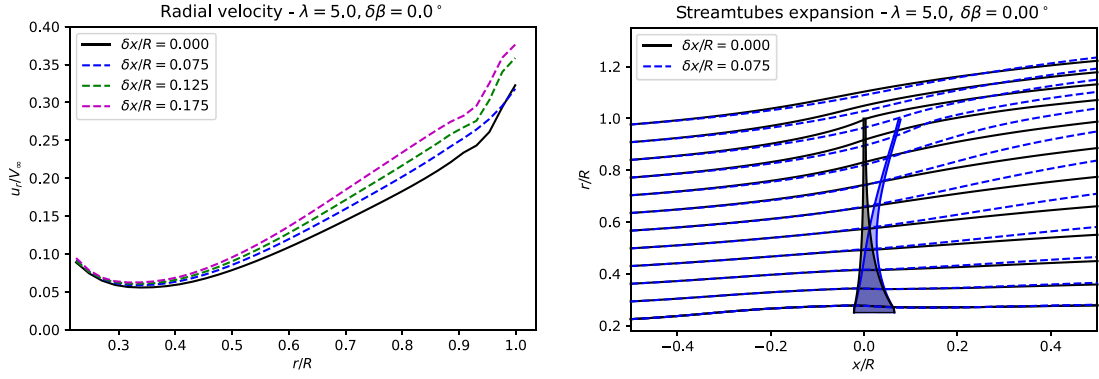


Fig. 12. Spanwise distribution of radial velocity u_r/V_∞ for different values of flapwise deformation (left) and comparison of annular streamtubes passing the blade for two flapwise deformation cases (right). The shaded area in the streamtubes plot represents the outline of the undeformed (grey) and deformed (blue) rotors. Data in both plots correspond to a tip-speed ratio $\lambda = 5.0$. (For interpretation of the references to colour in this figure legend, the reader is referred to the web version of this article.)

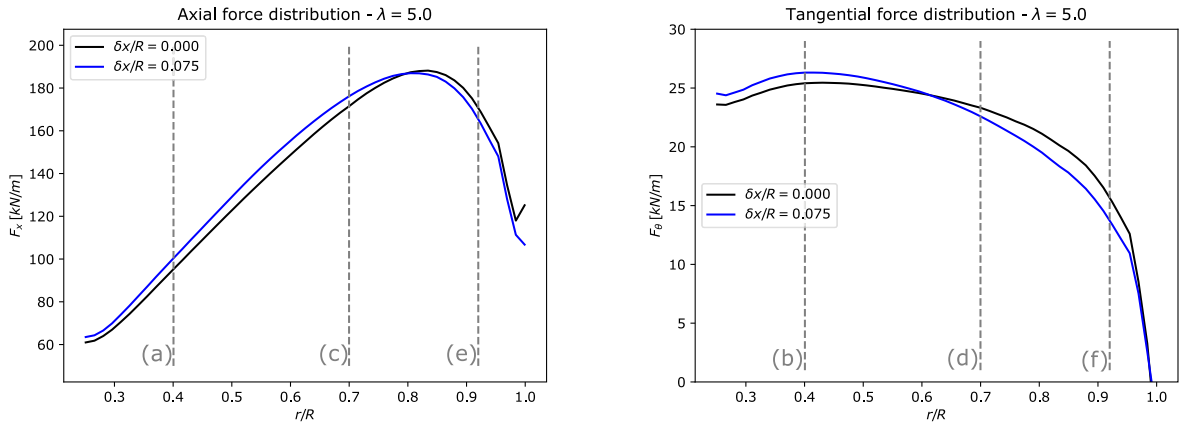


Fig. 13. Spanwise thrust (left) and tangential force (right) distribution comparison for the rotor with two different flapwise deformations ($\delta x/r = 0.000$ and $\delta x/r = 0.075$) at $\lambda = 5.0$. The vertical lines indicate the analysed radial locations and the letters are references to the corresponding sub-figures in Fig. 14.

The pressure drop effects can be observed in the CFD results. In Fig. 13 we present a comparison of the thrust and tangential force distributions for two typical cases, with and without flapwise-deformation at $\lambda = 5.0$. In each of these plots we include three vertical lines marking different locations on the blade span: the first lines (a and b) in a region where both thrust and tangential force increase with deformation, the second pair (c and d) show an area of the blade where thrust increases whilst the tangential force decreases, and the third pair (e and f) show the region where both thrust and tangential forces decrease. Whilst these plots show the case for $\lambda = 5.0$ the same observations can be made for different tip deformation $\delta x/R$ cases at all the analysed tip-speed ratios.

At the first analysed location, $r/R = 0.40$, we observe an increase in both thrust and tangential force. Fig. 14(a) and (b) show the cumulative chordwise distribution of the thrust and tangential force on this section. These plots show how the flapwise deformation pressure variations are localised on the suction (downstream) side of the blade. The plots also show how the thrust differences between deformed and undeformed blades are generated over most of the blade chord (increasing monotonically until approximately 80% of the chord), whereas the tangential force differences are generated over a smaller portion of the hydrofoil, between approximately 25% and 35% of chord, as a consequence of the suction increase but also due to the local foil geometry.

At $r/R = 0.70$, an increase in thrust and reduction in tangential force due to flapwise deformation is observed. Fig. 14(c) and (d) show that the differences are still concentrated on the suction side of the blade, and that these variations occur over a smaller portion of the chord for the thrust and concentrated towards the trailing edge. The tangential force shows a slight reduction for the deformed case that starts close to the leading edge.

Near the tip at $r/R = 0.92$, where three-dimensional flow effects and tip-loss phenomena are significant, Fig. 14(e) and (f) show that both thrust and tangential force are reduced with flapwise deformation.

The cumulative force plots (Fig. 14) are consistent with the static pressure reduction predicted by Eq. (14) for cases with flapwise deformation. The force changes are concentrated on the suction side of the blade, and are most evident

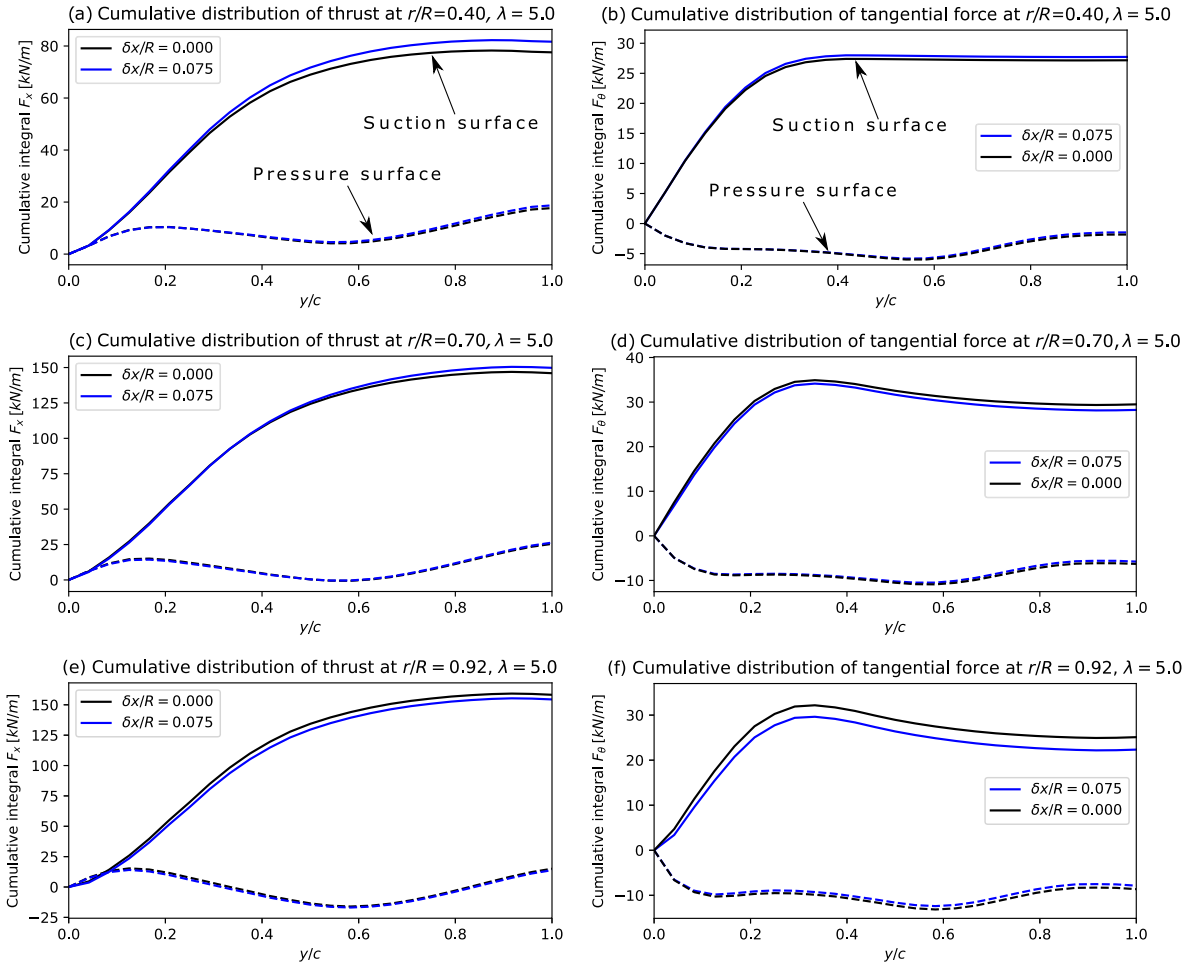


Fig. 14. Cumulative force distributions at $r/R = 0.40$, $r/R = 0.70$ and $r/R = 0.92$ for the undeformed and deformed $\delta x/R = 0.075$ cases at $\lambda = 5.0$. The continuous lines correspond to the suction surface and the dashed lines to the pressure surface of the blade, and y/c is the local chordwise coordinate.

around the inboard section of the blade, as observed for the $r/R = 0.40$ and $r/R = 0.70$ sections. As sections get closer to the tip, however, there is an increasing preponderance of the near-tip load shedding effect augmented by increased radial flow, as seen for the $r/R = 0.92$ section. This phenomenon is discussed in Section 5.2.2.

The pressure change around the suction side of the blade affects thrust and tangential force distributions differently. On the suction side of the blade any change in pressure, such as that created by flapwise deformation, will lead to a change in thrust. This is a result of geometry as most of the suction surface area is projected in the streamwise direction. However, the area projection of the suction surface in the tangential direction changes significantly with aerofoil shape and local twist angle. Consequently, depending on the chordwise distribution of the suction increase around the foil section and the local distribution of the tangentially projected area, the change in tangential force that occurs with blade deformation can be quite varied at different spanwise locations.

Fig. 15 (left) displays the change in the pressure coefficients on the suction side for the rigid and flapwise deformed blades at the analysed radial locations, with the pressure coefficients normalised by the local dynamic pressure $1/2\rho W^2$. A negative ΔC_{Pres} indicates an increase in suction for the deformed case relative to the undeformed case. Fig. 15 (right) shows the tangential-component of the blade's suction-side normal vector, \hat{n}_j ; positive \hat{n}_j is in the direction of positive torque generation, whilst negative \hat{n}_j is in the torque resisting direction. These plots show how the changes to the tangential force result from the interaction between the pressure differences induced by the flapwise deformation and the suction surface normal vector and tangentially-project area, which are a function of the hydrofoil shape and the blade twist (neither of which are affected by $\delta x/R$).

Fig. 15 shows that \hat{n}_j is mostly positive near the root, and hence the observed increase in suction results in an increase in the local tangential force. However, as we move towards the outboard section of the blade, $r/R = 0.70$, the change in twist distribution results in \hat{n}_j being positive towards the leading edge and negative towards the trailing edge of the

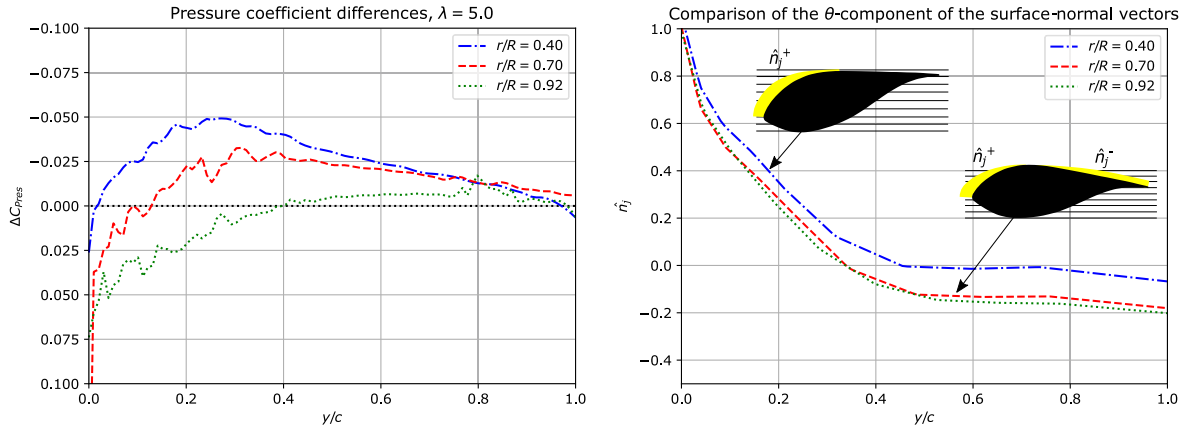


Fig. 15. Difference between the suction surface pressure coefficients of the $\delta x/R = 0.000$ and $\delta x/R = 0.075$ cases at different radial locations (left) and tangential-component of the blade's suction-side normal vector (\hat{n}_j) at the same radial locations (right). The right figure includes diagrams that highlight the magnitude of the tangential-normal vector \hat{n}_j over the chord at the two pointed radial locations, with the horizontal lines marking the tangential direction and the yellow zones showing the magnitude of \hat{n}_j . (For interpretation of the references to colour in this figure legend, the reader is referred to the web version of this article.)

hydrofoil. At this location a small but consistent increase in suction is observed across most of the blade chord. Hence there is a tangential force balance with increased torque contribution towards the leading edge and reduced torque contribution towards the trailing edge, with the overall balance being a very small decrease in local torque contribution once forces are integrated around the blade chord.

5.2.2. Radial loss augmentation

Returning to the force distributions in Fig. 9 we observe that, with increasing $\delta x/R$, the magnitude of the outboard load shedding is increased, and its onset is displaced inboard, affecting both the thrust and tangential force distributions. The observed effects are similar to those normally associated with tip losses.

The changes in force and pressure near the tip are related to three-dimensional flow variations. This complex flow phenomena can be analysed by examining the governing Navier–Stokes equations, focusing on the axial pressure gradient. We note that the underlying simulations assume steady state flow, and thus we neglect temporal derivatives in the momentum equations. Eq. (15) presents the axial-flow component of the Navier–Stokes equation in cylindrical coordinates, where u is a velocity component; p the static pressure; the indices x , θ and r the axial, tangential and radial coordinates respectively; and μ the fluid viscosity:

$$\rho \left(u_r \frac{\partial u_x}{\partial r} + \frac{u_\theta}{r} \frac{\partial u_x}{\partial \theta} + u_x \frac{\partial u_x}{\partial x} \right) = -\frac{\partial p}{\partial x} + \mu \left[\frac{1}{r} \frac{\partial}{\partial r} \left(r \frac{\partial u_x}{\partial r} \right) + \frac{1}{r^2} \frac{\partial^2 u_x}{\partial \theta^2} + \frac{\partial^2 u_x}{\partial x^2} \right] \quad (15)$$

We assume the viscous effects to be negligible outside the blade boundary layer where the following analysis will be applied, and thus we neglect the viscous term in Eq. (15). We seek an azimuthally-averaged analysis in the context of the Streamtube Analysis Method, and hence u_x , u_r and u_θ become the azimuthal-average of the velocity components. Thus, the circumferential gradients of azimuthally-averaged quantities are zero, i.e., $\partial u_x / \partial \theta = 0$. These assumptions result in:

$$\frac{\partial p}{\partial x} \approx -\rho \left(u_r \frac{\partial u_x}{\partial r} + u_x \frac{\partial u_x}{\partial x} \right) \quad (16)$$

for which the velocities and their gradients can be readily extracted from the simulations. The pressure gradient $\partial p / \partial x$ can then be integrated in the axial direction to obtain an approximation of the pressure p^* (relative to a constant p_0) as a function of the axial-coordinate x for each radial coordinate:

$$p^* = \int \frac{\partial p}{\partial x} dx + p_0 = -\rho \int \left(u_r \frac{\partial u_x}{\partial r} + u_x \frac{\partial u_x}{\partial x} \right) dx + p_0 \quad (17)$$

The integral of Eq. (17) can be evaluated in two branches, upstream and downstream of the rotor, to avoid the large gradients that occur near to the rotor plane, and where the neglected terms in Eq. (16) are likely to be significant. Fig. 16 shows a comparison of the pressure p extracted from CFD simulations and the estimated pressure p^* for two different flapwise deformation cases, showing good agreement at distances greater than $\pm 0.1R$ away from the blade.

By evaluating the pressure, p^* , through the turbine at different radial locations, the thrust distribution per unit span can be estimated, as in classical momentum theory, from the difference in static pressure between the upstream and downstream sides of the rotor plane, p^{*+} and p^{*-} :

$$F_x(r) \approx F_x^*(r) = (p^{*+} - p^{*-}) 2\pi r \quad (18)$$

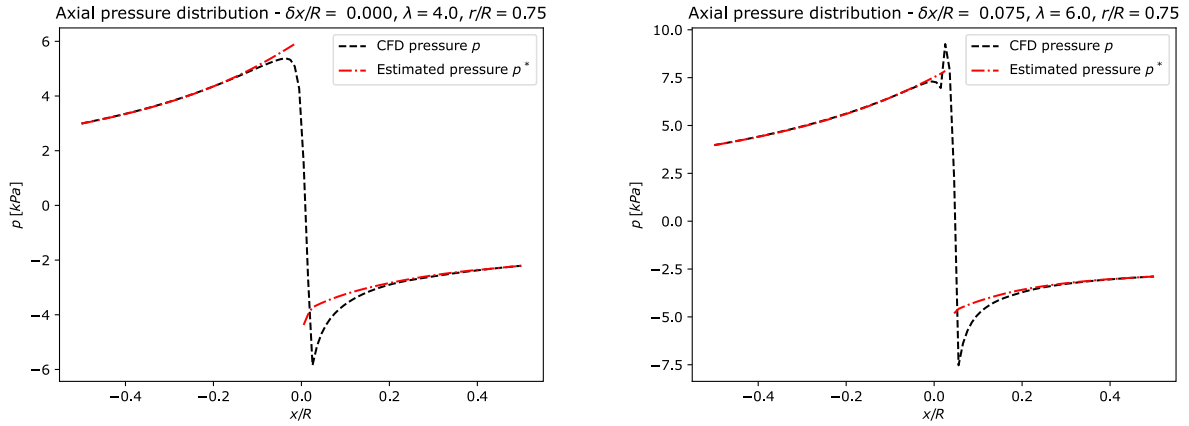


Fig. 16. Comparison of the pressure extracted from CFD simulation, p , and the approximation p^* for two illustrative cases; left, rigid blade at a tip-speed ratio $\lambda = 4.0$; right, deformed blade ($\delta x/R = 0.075$) at $\lambda = 6.0$.

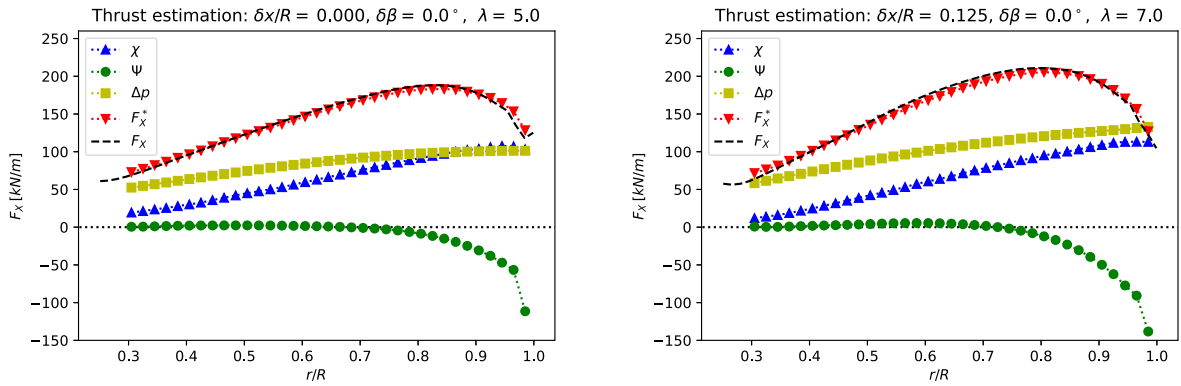


Fig. 17. Verification of the thrust estimation on a rotor blade based on Eqs. (19)–(21) comparing it to the force calculated by integrating pressure and shear stresses on the blade surface for undeformed $\delta x/R = 0.000$ and deformed $\delta x/R = 0.125$ cases at $\lambda = 5.0$ and $\lambda = 7.0$, respectively. The plots display the thrust approximation F_x^* as well as the constituents χ , the change in axial momentum, ψ , the radial loss, and Δp , the difference in static pressure from upstream to downstream of the rotor.

Eq. (18) can be decomposed into the contributions from the change in axial momentum:

$$\chi = -2\pi r \rho \left(\int_{-h}^{0^+} u_x \frac{\partial u_x}{\partial x} dx - \int_{+h}^{0^-} u_x \frac{\partial u_x}{\partial x} dx \right), \quad (19)$$

the radial loss which we define as:

$$\psi = -2\pi r \rho \left(\int_{-h}^{0^+} u_r \frac{\partial u_x}{\partial r} dx - \int_{+h}^{0^-} u_r \frac{\partial u_x}{\partial r} dx \right), \quad (20)$$

and a contribution from the difference in static pressure Δp from a distance h upstream and downstream of the rotor plane. Hence we determine an estimate to the spanwise variation in axial thrust through:

$$F_x^* = \chi + \psi + 2\pi r \Delta p \quad (21)$$

Fig. 17 shows a comparison between the thrust estimation F_x^* and the thrust calculated by integrating pressure and shear stress over the blade surfaces F_x for example undeformed and deformed cases. Alongside the force estimations, the contributions from χ , ψ and Δp are provided. These figures show how F_x^* provides a good description of the thrust force on the blade for cases with and without flapwise deformation. The approximation enables the quantification and further inspection of the main terms driving the forces on the blade.

The difference between the integration constants, Δp , is plotted in Fig. 17. Over the axial distance used to integrate the axial pressure estimation ($x/R = \pm h/R = \pm 0.5$), a static pressure difference was observed which was evaluated directly from the CFD simulations. If the gradient was integrated at sufficient distance from the rotor in unblocked conditions, the static pressure is expected to be the same far upstream and far downstream of the rotor, and so $\Delta p \rightarrow 0$ as $h \rightarrow \infty$.

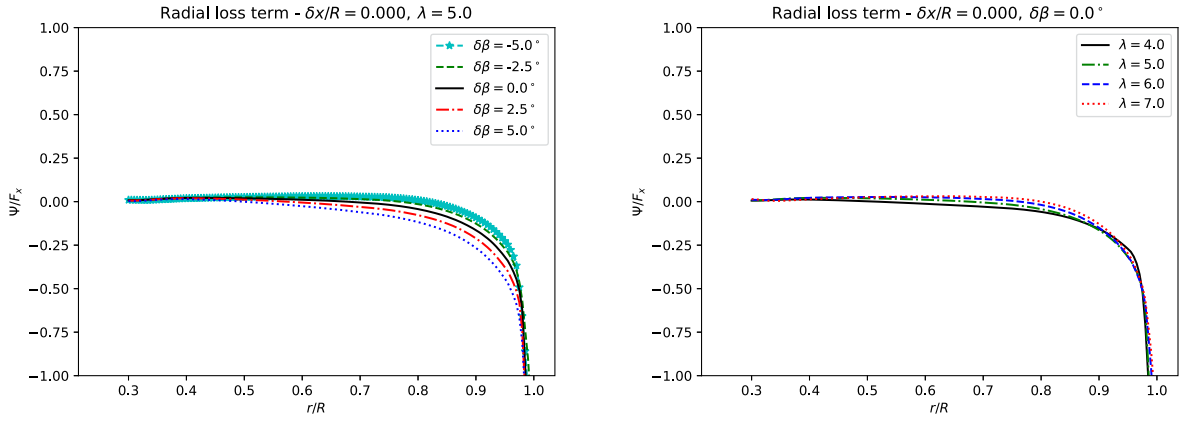


Fig. 18. Changes in the non-dimensional radial loss term for different twist deformations $\delta\beta$ cases at $\lambda = 5.0$ (left) and the undeformed rotor at different tip-speed ratios (right).

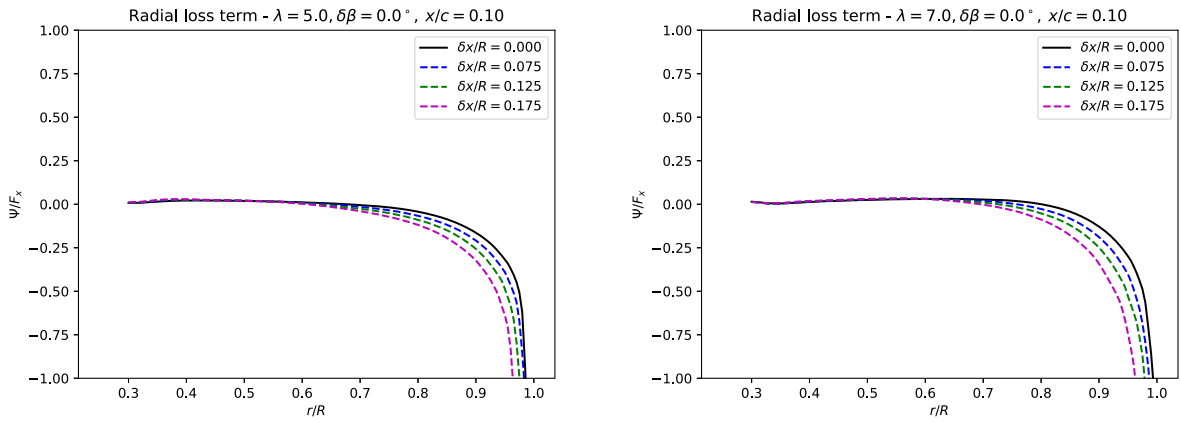


Fig. 19. Changes in the non-dimensional radial loss term for different flapwise deformation $\delta x/R$ cases at $\lambda = 5.0$ (left) and $\lambda = 7.0$ (right).

Fig. 17 also shows that the terms χ and ψ act in different directions. χ represents changes in axial momentum, and contributes to thrust generation, whilst ψ represents the loss or leakage of axial momentum due to three-dimensional radial flow effects, and captures near-tip load-shedding effects.

The radial loss ψ is similar in shape to the models used to correct for tip-losses in BEMT (e.g., Glauert (1947) and Wimshurst and Willden (2017a)). Here though ψ encapsulates both the tip-losses as well as the load reduction associated with radial flow. In particular, in the absence of flapwise deformation, the radial loss has a negligible effect on the inboard region and starts increasing in an exponential-like manner close to the tip, similar to conventional tip-loss models.

In Figs. 18 and 19 we examine the variation of the radial loss term, presented as a fraction of the local thrust force. We note that ψ/F_x may go below -1 near the blade tip to balance the radially increasing contributions of χ/F_x and Δp , which collectively result in a reduction in magnitude of F_x but maintain an overall positive value. We examine the form of the radial losses for different cases of blade twist deformation $\delta\beta$ and flapwise deformation $\delta x/R$, and with tip-speed ratio λ for an undeformed blade.

The plots show that negative blade twist deformation reduces the radial loss whilst positive blade twist increases the loss. A small dependency on λ for the undeformed blade is also observed. In the absence of flapwise deformations, and despite changes in radial loss magnitude across the inboard of the blade, the radial losses converge near the tip at approximately $r/R = 0.98$ for all the λ and $\delta\beta$ cases.

Fig. 19 shows that the radial loss term increases with flapwise deformation, with the onset of the radial loss moving inboard along the blade as tip deformation increases. This confirms that the reductions in near-tip loads in cases with flapwise deformation are a consequence of the spanwise flow effects induced by this deformation component.

Larger radial losses with flapwise deformation result in the reduction in pressure difference between suction and pressure surfaces of the blade near the tip, as observed in the cumulative force distributions (Fig. 14). Here we note that any increase in suction surface pressure caused by downstream wake expansion is offset, near the tip, by the increase in radial loss as the tip is approached, and hence the overall thrust and tangential forces decrease in the near tip region.

5.2.3. Influence of the flapwise deformation on two-dimensional polar coefficients

The inboard load augmentation and the increased radial losses affect how the hydrodynamic forces develop on the blade. Although these are three-dimensional flow phenomena it is instructive to interpret the flow-field changes in terms of changes to two-dimensional sectional blade characteristics, as these are most normally used in the design and analysis of rotors. Fig. 20 shows the blade sectional lift and drag coefficients, as well as the foil efficiency C_L/C_D , computed from analysis of the different simulated flapwise deformation cases at four radial stations and presented as functions of the local angle of attack α , which is itself not known a priori and is an output of the flow-field analysis.

As the blade deforms we observe that the sectional lift coefficients increase for inboard sections of the blade and reduce towards the tip, across all the analysed angles of attack. This is a consequence of the inboard load augmentation and the radial loss. The shape and slope of the C_L curves as functions of α remain similar between the $\delta x/R$ cases at equivalent radial locations. However, the vertical offsets of these curves change as functions of radial position, r/R , and deformation, $\delta x/R$.

A monotonic increase of C_L with increasing flapwise deformation is observed on inboard blade sections until around $r/R = 0.70$, where the trend starts to change. There, we observe an increase in C_L for $\delta x = 0.075$, plateauing for higher values of $\delta x/R$. Finally, near the tip, we observe that the lift coefficient is reduced with increasing flapwise deformation. The differences between the undeformed and deformed cases, for $C_L(\alpha)$, generally show a stronger dependency on r/R and $\delta x/R$ than on α itself.

For the drag coefficient, we observe that the difference between the undeformed and deformed cases shows a stronger dependency on the angle of attack, increasing towards larger values of α , as well as displaying a monotonic increase with $\delta x/R$ for the entire blade span.

Only a small gain in hydrofoil efficiency is observed for the deformed cases at low angles of attack on sections closer to the root of the blade. However, most of the observed changes in lift and drag have a dramatic impact on foil efficiency in the outboard half of the blade across the entire α range, related to the rotor performance loss due to the flapwise deformation.

These changes in efficiency also show that the lift and drag coefficients change in different proportions as functions of the angle of attack (i.e., changes in tip-speed ratio), flapwise deformation and radial location. If correction factors are to be developed and included in engineering models based on two-dimensional aerofoil theory, separate correction factors should be generated either for the lift and drag coefficients, or for the tangential and thrust coefficients, as has been previously suggested by Wimshurst and Willden (2018) for the development of tip-loss correction factors.

6. Conclusions

Our work presents a novel insight into the hydrodynamic mechanisms driving thrust and power changes in deforming rotor blades. We have highlighted the importance of twist and flapwise deformations and the role of spanwise flows on predicting the load distribution along deformed blades.

Twist deformations cause a substantial change to the blade loading and performance, even for small angles of deformation. These changes are straightforward to analyse using two-dimensional blade-element theory for modest twist angles, as it provides a framework which predicts the hydrodynamic effects of changing the twist angle distribution through polar lift and drag coefficients.

Flapwise deformations, which cannot be analysed through blade element theory, also affect rotor blade hydrodynamics. Substantial modifications to the spanwise thrust distribution occur due to flapwise deformations, but the impact on the integrated thrust is limited due to the presence of two opposing hydrodynamic mechanisms: inboard load augmentation and an increase in near-tip load shedding with flapwise deformation.

The inboard load augmentation is caused by a reduction in static pressure on the suction side of the blade. This is generated by the increased radial force acting on the blade due to changes in the surface-normal orientation as a consequence of blade deformation, which induces an outwards radial flow velocity, driving greater wake expansion. This change in wake expansion results in a static pressure drop on the downstream side of the rotor, increasing lift and drag forces, with a larger relative increase for the latter and consequent reduction in foil efficiency across much of the blade. This effect and its causes, to the best of our knowledge, have not previously been described in the literature.

The increase in near-tip load shedding is generated by the onset of three-dimensional flow effects moving inboard along the blade, reducing both thrust and torque due to faster static pressure equalisation between both sides of the blade near the tip. This phenomenon was characterised and quantified through the radial loss analysis, and is in qualitative agreement with results presented by Crawford (2006) and Mikkelsen et al. (2001) that show an increasing thrust shedding as the tip is approached for cases with downstream coning.

The inboard load augmentation and near-tip load shedding mechanisms observed with the flapwise deformation also affect the tangential force, but with more pronounced force reductions across a greater part of the span, thus significantly affecting the integrated power. These results are in disagreement with those presented by Madsen and Rasmussen (1999) and Mikkelsen et al. (2001) regarding the invariability of the power coefficient with rotor coning, and is explained by methodological differences. The actuator disc model, as opposed to the blade-resolved simulations used in our study, is unable to capture the geometry- and location-dependent changes in tangential force that affect power performance.

The impact of flapwise deformations on reducing hydrofoil efficiency and rotor performance could enable power shedding through blade deformations if coupled with suitable control strategies. This topic, alongside with a study on the interactions between coupled flapwise and twist deformations, will be addressed in future work.

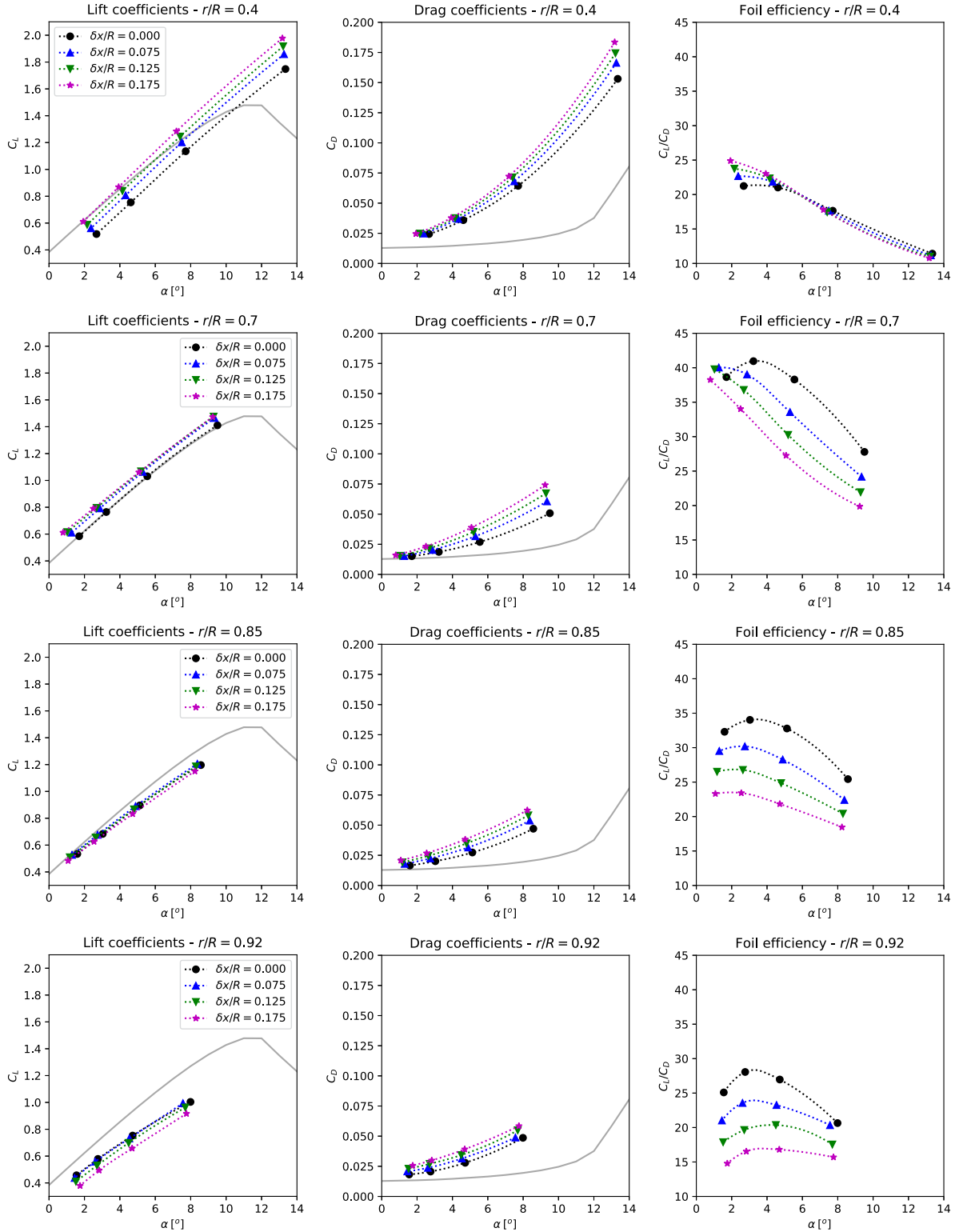


Fig. 20. Lift, drag and aerofoil efficiency (lift-to-drag ratio) at different radial locations for various flapwise-deformation cases. Values calculated using the SAM with $x/c = 1.0$. Note that each simulated tip-speed ratio case provides foil data at a single α at the corresponding radial location. The grey line corresponds to the two-dimensional lift and drag coefficients.

CRediT authorship contribution statement

Federico Zilic de Arcos: Conceptualization, Methodology, Software, Formal analysis, Investigation, Data curation, Writing – original draft. **Christopher R. Vogel:** Conceptualization, Methodology, Formal analysis, Resources, Supervision, Writing – reviewing & editing. **Richard H.J. Willden:** Conceptualization, Methodology, Formal analysis, Resources, Supervision, Writing – reviewing & editing.

Declaration of competing interest

The authors declare that they have no known competing financial interests or personal relationships that could have appeared to influence the work reported in this paper.

Acknowledgements

This work was supported in part by CONICYT PFCHA/BECAS CHILE DOCTORADO EN EL EXTRANJERO 2016/72170292. RHJW would like to acknowledge EPSRC, UK who support his fellowship through grant number EP/R007322/1. The authors would also like to acknowledge the use of the University of Oxford Advanced Research Computing (ARC) facility in carrying out this work. <http://dx.doi.org/10.5281/zenodo.22558>.

References

- Afgan, I., McNaughton, J., Rolfo, S., Apsley, D., Stallard, T., Stansby, P., 2013. Turbulent flow and loading on a tidal stream turbine by LES and RANS. *Int. J. Heat Fluid Flow* 43, 96–108.
- Zilic de Arcos, F., Willden, R., Vogel, C., 2018. Hydroelastic modelling of composite tidal turbine blades. In: *Advances in Renewable Energies Offshore - Proceedings of 3rd International Conference on Renewable Energies Offshore (RENEW 2018)*. Lisbon.
- Bazilevs, Y., Hsu, M.-C., Kiendl, J., Wüchner, R., Bletzinger, K.-U., 2011. 3D Simulation of wind turbine rotors at full scale. Part II: Fluid-structure interaction modeling with composite blades. *Internat. J. Numer. Methods Fluids* 65:236–254.
- Bir, G.S., 2001. Computerized method for preliminary structural design of composite wind turbine blades. *J. Solar Energy Eng.* 123 (4), 372. <http://dx.doi.org/10.1115/1.1413217>.
- Boorsma, K., Schepers, J., 2014. New MEXICO experiment: Preliminary overview with initial validation. *Energy Research Centre of the Netherlands (ECN)*.
- Burton, T., Jenkins, N., Sharpe, D., Bossanyi, E., 2011. *Wind Energy Handbook*. John Wiley & Sons.
- Chehouiri, A., Younes, R., Ilinca, A., Perron, J., Coe, M., 2015. Review of performance optimization techniques applied to wind turbines. *Appl. Energy* 142, 361–388. <http://dx.doi.org/10.1016/j.apenergy.2014.12.043>.
- Crawford, C., 2006. Re-examining the precepts of the blade element momentum theory for coning rotors. *Wind Energy Int. J. Progress Appl. Wind Power Convers. Technol.* 9 (5), 457–478.
- Fluent, ANSYS, 2018. *ANSYS Fluent theory guide 19.0*. ANSYS, Canonsburg, PA.
- Gant, S., Stallard, T., 2008. Modelling a tidal turbine in unsteady flow. In: *Proceedings of the Eighteenth (2008) International Offshore and Polar Engineering Conference*, 2007, pp. 473–479.
- Glauert, H., 1947. *The Elements of Aerofoil and Airscrew Theory*. Cambridge University Press.
- Grogan, D.M., Leen, S.B., Kennedy, C.R., Brádaigh, C.M.O., 2013. Design of composite tidal turbine blades. *Renew. Energy* 57, 151–162. <http://dx.doi.org/10.1016/j.renene.2013.01.021>.
- Guntur, S., Jonkman, J.M., Jonkman, B., Wang, Q., Sprague, M.A., Hind, M., Sievers, R., Schreck, S.J., 2016. Fast v8 verification and validation for a MW-scale wind turbine with aeroelastically tailored blades. In: *34th Wind Energy Symposium*. p. 1008.
- Hunter, W., 2015. *Actuator disk methods for tidal turbine arrays* (Ph.D. thesis). University of Oxford.
- Kaufmann, N., Carolus, T.H., Starzmann, R., 2019. On the effect of elastic blade deformation on the performance of a horizontal axis tidal current turbine. In: *Proceedings of the Thirteenth European Wave and Tidal Energy Conference*. EWTEC, ISSN: 2309-1983.
- Larsen, T.J., Hansen, A.M., 2007. *How 2 HAWC2, the user's manual*.
- Lobitz, D.W., Veers, P.S., 2003. Load mitigation with bending/twist-coupled blades on rotors using modern control strategies. *Wind Energy Int. J. Progress Appl. Wind Power Convers. Technol.* 6 (2), 105–117.
- Luo, J., Gosman, A., 1994. Prediction of impeller-induced flow in mixing vessels using multiple frames of reference. *INSTITUTE OF CHEMICAL ENGINEERS SYMPOSIUM SERIES*.
- Madsen, H.A., Rasmussen, F., 1999. The influence on energy conversion and induction from large blade deflections. In: *EWEC-CONFERENCE*. pp. 138–141.
- McNaughton, J., Rolfo, S., Apsley, D., Afgan, I., Stallard, T., Stansby, P., 2012. CFD prediction of turbulent flow on an experimental tidal stream turbine using RANS modelling. In: *1st Asian Wave and Tidal Energy Conference*.
- Menter, F.R., 1994. Two-equation eddy-viscosity turbulence models for engineering applications. *AIAA J.* 32 (8), 1598–1605.
- Menter, F.R., Kuntz, M., Langtry, R., 2003. Ten years of industrial experience with the SST turbulence model. *Turbulence Heat Mass Transfer* 4, 625–632. <http://dx.doi.org/10.4028/www.scientific.net/AMR.576.60>.
- Mikkelsen, R., Sørensen, J.N., Shen, W.Z., 2001. Modelling and analysis of the flow field around a coned rotor. *Wind Energy* 4 (3), 121–135. <http://dx.doi.org/10.1002/we.50>.
- Murray, R.E., Ordonez-Sanchez, S., Porter, K.E., Doman, D.A., Pegg, M.J., Johnstone, C.M., 2018. Towing tank testing of passively adaptive composite tidal turbine blades and comparison to design tool. *Renew. Energy* 116, 202–214. <http://dx.doi.org/10.1016/j.renene.2017.09.062>.
- Nicholls-Lee, R., 2011. *Adaptive Composite Blades for Horizontal Axis Tidal Turbines* (Ph.D. thesis). University of Southampton.
- Nicholls-Lee, R.F., Turnock, S.R., Boyd, S.W., 2013. Application of bend-twist coupled blades for horizontal axis tidal turbines. *Renew. Energy* 50, 541–550. <http://dx.doi.org/10.1016/j.renene.2012.06.043>.
- Rafiee, R., Tahani, M., Moradi, M., 2016. Simulation of aeroelastic behavior in a composite wind turbine blade. *J. Wind Eng. Ind. Aerodyn.* 151, 60–69. <http://dx.doi.org/10.1016/j.jweia.2016.01.010>.
- Roache, P.J., 1994. Perspective: A method for uniform reporting of grid refinement studies. *J. Fluids Eng.* 116 (3), 405–413. <http://dx.doi.org/10.1115/1.2910291>.

- Schepers, J., Boorsma, K., Cho, T., Gomez-Iradi, S., Schaffarczyk, P., Jeromin, A., Lutz, T., Meister, K., Stoevesandt, B., Schreck, S., et al., 2012. Final report of IEA Task 29, Mexnet (Phase 1): analysis of Mexico wind tunnel measurements. Energy Research Centre of the Netherlands (ECN),
- Schluntz, J., Willden, R., 2015. The effect of blockage on tidal turbine rotor design and performance. *Renew. Energy* 81, 432–441.
- Vorpahl, F., Strobel, M., Jonkman, J.M., Larsen, T.J., Passon, P., Nichols, J., 2014. Verification of aero-elastic offshore wind turbine design codes under IEA wind task XXIII. *Wind Energy* 17 (4), 519–547.
- Wada, H., Murayama, H., Minami, Y., Uzawa, K., Kageyama, K., 2011. Deformation evaluation of elastic composite blade models for tidal power generation by fluid–structure interaction analysis. In: 18th International Conference on Composite Materials.
- Wang, L., Liu, X., Kolios, A., 2016. State of the art in the aeroelasticity of wind turbine blades: Aeroelastic modelling. *Renew. Sustain. Energy Rev.* 64, 195–210. <http://dx.doi.org/10.1016/j.rser.2016.06.007>.
- Wimshurst, A., Willden, R., 2016. Computational analysis of blockage designed tidal turbine rotors. In: *Progress in Renewable Energies Offshore - Proceedings of 2nd International Conference on Renewable Energies Offshore, RENEW 2016*, Emec. pp. 587–597.
- Wimshurst, A., Willden, R., 2017a. Analysis of a tip correction factor for horizontal axis turbines. *Wind Energy* 20 (9), 1515–1528.
- Wimshurst, A., Willden, R.H.J., 2017b. Extracting lift and drag polars from blade-resolved computational fluid dynamics for use in actuator line modelling of horizontal axis turbines. *Wind Energy* 20 (5), 815–833. <http://dx.doi.org/10.1002/we.2065>, arXiv:arXiv:1006.4405v1.
- Wimshurst, A., Willden, R., 2018. Computational observations of the tip loss mechanism experienced by horizontal axis rotors. *Wind Energy* 21 (7), 544–557.
- Zilic de Arcos, F., Tampier, G., Vogel, C.R., 2020a. Numerical analysis of blockage correction methods for tidal turbines. *J. Ocean Eng. Mar. Energy* 6 (2), 183–197. <http://dx.doi.org/10.1007/s40722-020-00168-6>.
- Zilic de Arcos, F., Vogel, C., Willden, R., 2019. Hydrodynamic modelling of flexible tidal turbine blades. In: *Proceedings of the Thirteenth European Wave and Tidal Energy Conference. EWTEC*, ISSN: 2309-1983.
- Zilic de Arcos, F., Vogel, C., Willden, R., 2020b. Extracting angles of attack from blade-resolved rotor CFD simulations. *Wind Energy* 23 (9), 1868–1885. <http://dx.doi.org/10.1002/we.2523>.